

Multiple Resonance Deep-red Emitters with Hybridized π -bonding/ non-bonding Orbitals to Surpass the Energy Gap Law

Yuewei Zhang

Tsinghua University

Dongdong Zhang

Tsinghua University

Tianyu Huang

Tsinghua University

Alexander Gillett

Cambridge University <https://orcid.org/0000-0001-7572-7333>

Yang Liu

Sichuan University

Linsong Cui

University of Cambridge <https://orcid.org/0000-0001-6577-3432>

Zhengyang Bin

Sichuan University

Guomeng Li

Tsinghua University

Chen Zhang

Tsinghua University

Yang Lu

Tsinghua University

Ziyang Liu

Tsinghua University

Jinbei Wei

Chinese Academy of Sciences

Lian Duan (✉ duanl@mail.tsinghua.edu.cn)

Tsinghua University

Article

Keywords: optics, energy gap law, diode

Posted Date: January 11th, 2021

DOI: <https://doi.org/10.21203/rs.3.rs-119314/v1>

License:   This work is licensed under a Creative Commons Attribution 4.0 International License.

[Read Full License](#)

Abstract

Efficient organic emitters in the deep-red to near infrared region are rare due to the 'energy gap law'. Here, multiple boron (B)- and nitrogen (N)-atoms embedded polycyclic heteroaromatics featuring hybridized π -bonding/ non-bonding molecular orbitals are constructed, providing a way to overcome the above luminescent boundary. The introduction of B-phenyl-B and N-phenyl-N structures enhances the electronic coupling of those para-positioned atoms, forming restricted π -bonds on the phenyl-core for delocalized excited states and thus a narrow energy gap. The mutually ortho-positioned B- and N-atoms also induce a multiple resonance effect on the peripheral skeleton for the non-bonding orbitals, creating shallow potential energy surfaces to eliminate the high-frequency vibrational quenching. The corresponding deep-red emitters with peaks at 662 nm and 692 nm exhibit narrow full-width at half-maximums of 38 nm, high radiative decay rates of $\sim 10^8 \text{ s}^{-1}$, $\sim 100\%$ photo-luminescence quantum yields and record-high maximum external quantum efficiencies of $>28\%$ in a normal planar organic light-emitting diode structure, simultaneously.

Introduction

The energy gap law^{1,2}, recognized as the fact that nonradiative transitions will significantly increase with the decreased energy gap, has created a formidable barrier to produce deep-red (DR)/ near-infrared (NIR) organic emitters with high photo-luminescence quantum yields (PLQYs), despite their great demand for applications in night vision displays, biomedical imaging, optical communications and computing³⁻⁷. This effect is strong even for rigid systems, as was observed in the nonradiative deactivation of polycyclic aromatic hydrocarbons (PAHs)⁸. In those large conjugation PAH structures, the highest occupied and lowest unoccupied molecular orbitals (HOMO and LUMO, respectively) are primarily localized between atoms, forming π -bonds with bonding/antibonding character. The resulted interactions between the electronic and nuclear vibrational motion will induce significant C=C torsion or C-H vibration with high frequency, forming deep potential energy surfaces (PES) as illustrated in Fig. 1a. In the absence of a zero-order surface crossing, such deep PES will facilitate the wavefunction overlap of the zero-vibration level (ν_0) of the excited state (singlet or triplet, that is S_1 or T_1) and the high isoenergetic vibration level (ν_n) of the ground state (S_0), consequently relaxing the excited states in a nonradiative decay pathway. For DR/NIR emitters with emission peaks $>650 \text{ nm}$, the small energy gap between ν_0 s (ΔE_{ν_0-0}) of S_1 (or T_1) and S_0 will exponentially accelerate this nonradiative transitions since only a few vibrational ladders in S_0 are required to satisfy the energy requirement for vibronic coupling with ν_0 of excited states, drastically reducing the emission intensity^{9,10}.

Fig. 1 | Relationship between PES and excited states decay processes. a, Scheme of excited states decay processes of PAHs with π -bonding and deep PES. In this type emitters, only a few vibrational ladders in S_0 are required to satisfy the energy requirement for vibronic coupling with ν_0 of S_1 , drastically increasing nonradiative transitions and reducing the emission intensity. b, Scheme of excited states decay processes of MR TADF emitters with non-bonding and shallow PES. In this type emitters, owing to the reduced

vibrational frequency, it is hard for vibrational ladders in S_0 to reach the energy requirement for vibronic coupling with ν_0 of S_1 , thus benefiting to eliminate nonradiative transitions.

Breakthroughs to surpass energy gap law have been made in planar platinum (Pt) complexes with dimers or oligomers to increase the exciton delocalization length, which can decouple the exciton band from high vibrational ladders in S_0 state and thus suppress nonradiative transitions^{11,12}. This conceptually advancements in molecular design leads to NIR-emitters with impressive PLQYs of over 80% under emission peaks of 740 nm and high performance NIR organic light-emitting diodes (OLEDs). Recently, DR/NIR thermally activated delayed fluorescence (TADF) emitters with PLQYs >80% and peaks at ~650 nm have also been reported¹³⁻¹⁶. Determined by the onset of their wide emission spectra, the relatively larger ΔE_{ν_0-0} s of TADF emitters than PAHs with similar emission peaks are beneficial for suppressing the nonradiative transitions, though at the cost of the color purity. On the other hand, the charge transfer features of TADF emitters would always lead to large reorganization energies (λ s) due to the large structure relaxation and thus much smaller radiative decay rates (k_r s) than that of PAHs. Therefore, it remains challenging to develop high color purity DR/NIR emitters with PLQYs up to 100%.

Quite recently, a new class of boron (B)- and nitrogen (N)-atoms embedded PAHs have been reported by Hatakeyama et al, in which the ortho-positioned electron donating N-atom and electron deficient B-atom induce complementary multiple resonance (MR) effects for the offset electron density distributions of HOMO and LUMO orbitals by one atom in an alternating pattern¹⁷⁻²⁶. Such MR emitters not only inherit the merits of small λ s of PAHs for high k_r s, but also minimizes the bonding/antibonding character between adjacent atoms. The so-called non-bonding character could significantly lower the vibration frequency in the molecules, leading to shallow PES of S_0 and S_1 states. In this regard, emitters with sharp photo-luminescence (PL) and electro-luminescence (EL) emissions can be expected. From another perspective, as illustrated in Fig.1b, for such shallow PES, more vibrational ladders in S_0 are required to reach the vibronic coupling with ν_0 of S_1 state, which is almost prohibited owing to their non-bonding characters, even for DR/NIR emitters. As a result, the high-frequency vibrational quenching can be theoretically eliminated in well-designed MR emitters, providing a way to surpass the energy gap law (Supplementary Fig. 1 and Supplementary Tables 1-2). Another bonus is that the alternated distributions of HOMO and LUMO render small energy gaps (ΔE_{ST} s) between S_1 and T_1 levels in these compounds and thus efficient TADF emissions.

Results

For organic emitters, extending the π -conjugation length is an effective way to redshift the emission. The non-bonding characters in MR-TADF emitters, however, would limit the increasement of conjugation even with enlarged planar structures, making it challenging for DR/NIR emission.^{17,20} Enhancing the CT character in MR-TADF emitters is an alternative way to achieve redshifted emissions, which however, would weaken the MR effect and thus broadening the emission spectra²². To fulfill the requirement of a small energy gap and a narrow emission bandwidth simultaneously, a multiple boron (B) and nitrogen (N)

atoms embedded polycyclic heteroaromatic motif was proposed here, enabling multiple B and N centers and the modulation of their arrangement around a central phenyl ring. As illustrated in Fig.2a, besides the mutually ortho-positioned B and N atoms, which is the basic requirement for MR effect, linear B-phenyl-B and N-phenyl-N structures were adopted. Previous works have demonstrated the formation of intramolecular dimeric radical between donors (or acceptors) in para positions due to the enhanced electronic coupling between a cation (or an anion) and a neutral moiety in linearly position^{27,28}. The resulted delocalized excited states will significantly narrow energy gap and thus facilitating red-shifted emission. The distributions of frontier energy levels were calculated and it was interesting to note that on the central phenyl ring, both HOMO and LUMO showed π -bond characters (Fig.2b), which arises from the coupling of electrons on para-positioned N atoms or B atoms as described above. The mutually ortho-positioned B and N atoms, meanwhile, induce MR effect on the peripheral skeleton, leading to the localization and separation of the HOMO and LUMO on different atoms. These non-bonding characters facilitate to lower vibration frequency for shallow PES in molecules as aforementioned and thus eliminate nonradiative transitions. The targeted emitters with hybridized π -bonding/ nonbonding molecular orbitals thereof possess the potential to fundamentally overcome the luminescent boundary set by the energy gap law. The energy gaps of the two targeted emitters were predicted by the time-dependent density functional theory (TD-DFT) calculations, obtaining small S_1 values of 2.01 eV and 2.07 eV for R-BN and R-TBN, respectively (Supplementary Tables 3).

Fig. 2 | Molecular design strategy of DR/NIR MR-TADF emitters. a, Scheme of the formation of delocalized excited states with B-phenyl-B and N-phenyl-N structures. b, The comparison between conventional PAH, MR-TADF emitters with and without B-phenyl-B and N-phenyl-N structures. For conventional PAH, taking 3,8,13,18-tetraphenylbenzo[5,6]indeno[1,2,3-cd]benzo[5,6]indeno[1,2,3-lm]perylene (DBP) as an example, π -bonds molecular orbitals can be observed. For MR-TADF emitters without B-phenyl-B or N-phenyl-N structures, non-bonding orbitals are obtained.

Additionally, the geometric changes of molecular conformation between S_0 and S_1 states and structural relaxation at the S_1 state are extremely small with reorganization (λ_S) / structural relaxation (λ_S^*) energies were calculated to be merely 0.10 and 0.09 eV, 0.08 and 0.08 eV for R-BN and R-TBN, respectively (Supplementary Figs. 2-4), significantly smaller than typical DR/NIR organic molecules (0.26-0.52 eV)^{12,29}. Those extremely small λ_S and λ_S^* facilitate narrow bandwidth emission with high radiative transitions and thigh oscillator strength (f) values of 0.25 and 0.33 for R-BN and R-TBN were obtained, respectively. Moreover, similar reference material with multiple B, N atoms but not linear N-phenyl-N and B-phenyl-B structure was also calculated and only nonbonding characters as well as a large S_1 energy of 2.9 eV were obtained, suggesting the N-phenyl-N and B-phenyl-B structure motif is essential for the formation of delocalized excited states. (Fig.2b)²⁶

Fig. 3 | Structure and photophysical properties of R-BN and R-TBN. a, ORTEP drawing of R-BN (up) and R-TBN (down) obtained by X-ray crystallographic analysis. Thermal ellipsoids are shown at 50% probability. Hydrogen atoms are omitted for clarity. b, UV/Vis absorption and fluorescence (298 K) spectra of R-BN

and R-TBN in toluene. c, Transient PL decay spectra of R-BN/R-TBN doped into CBP films (3 wt%) at room temperature. d, Transient absorption (TPA) spectra of R-BN (d) and R-TBN (e) doped in PMMA films (3 wt%) at room temperature.

Table 1 | Summary of the photophysical properties of R-BN and R-TBN.

	$S_1^{a)}$	$T_1^{a)}$	$\Delta E_{ST}^{a)}$	FWHM ^{a)}	HOMO ^{b)}	LUMO ^{c)}	PLQY ^{d)}	$\tau_{PF}^{d)}$	$\tau_{DF}^{d)}$	$k_r^{d)}$
	[eV]	[eV]	[eV]	[nm]	[eV]	[eV]		[ns]	[ms]	($10^7 s^{-1}$)
R-BN	1.87	1.69	0.18	38	-4.76	-3.06	100±2%	4.7	0.31	17
R-TBN	1.79	1.63	0.16	38	-4.69	-3.00	100±2%	10.3	0.71	7.1

^aMeasured in the toluene solution with a concentration of 10^{-5} mol/L. ^bMeasured in dry dichloromethane with a concentration of 10^{-3} mol/L. ^cMeasured in dry N,N-dimethylformamide with a concentration of 10^{-3} mol/L. ^dMeasured in 3 wt%-doped films of R-BN/R-TBN in CBP.

R-BN and R-TBN were synthesized in two steps from commercially available starting materials and no palladium or other transition metal catalysts were needed, making them cost effective. The single crystal X-ray diffraction analyses demonstrated that R-BN combines the characteristics of a fusion structure and a sterically hindered structure, where small torsional angles ($\sim 20^\circ$) of the carbazolyl groups could be found (Fig. 3a and Supplementary Fig. 5). This limited torsional flexibility can be another major factor in reducing the non-radioactive decay of R-BN/R-TBN. Photophysical properties of R-BN and R-TBN in toluene with a concentration of 10^{-5} M were measured and listed in Table 1. Strong absorption bands with a maximum at 629 nm ($\log \epsilon = 5.13$, where ϵ is the molar excitation coefficient) and 651 nm ($\log \epsilon = 4.87$) were recorded for R-BN and R-TBN, respectively (Fig. 3b and Supplementary Fig. 6). Arising from the small optical energy gaps of 1.87 eV and 1.79 eV for R-BN and R-TBN, deep red fluorescence emission peaked at 662 nm and 692 nm were observed, evidencing the molecular design strategy above. More importantly, nearly 100% PLQYs were measured for both emitters, suggesting the greatly suppressed nonradiative decay rates. Their small full-width at half-maximums (FWHMs) of both 38 nm reflect the narrow energy bandwidths of both S_0 and S_1 states as illustrated in Fig. 1b and thus the minimized the vibronic coupling between the S_0 and S_1 states. Also, small stokes shifts of 33 nm and 41 nm were also exhibited for R-BN and R-TBN, respectively, suggesting the limited vibrational relaxation at the S_1 state. All those parameters combined to overcome the limitation of energy gap law as aforementioned. The triplet energies were obtained from phosphorescence spectra recorded in a frozen toluene (77 K) matrix with a delay time of 10 ms, being 1.69 eV and 1.63 eV for R-BN and for R-TBN, respectively (Supplementary Fig. 10). The corresponding ΔE_{ST} values were 0.14 eV for R-BN and 0.17 eV for R-TBN. Such small ΔE_{ST} values are favorable for exciton up-conversion from T_1 to S_1 at ambient condition. These characteristics are promising for efficient DR/NIR emitters.

To evaluate the properties of TADF, PL properties of 3 wt% R-BN/R-TBN doped films with 4,4'-di(9H-carbazol-9-yl)-1,1'-biphenyl (CBP) as the wide-energy gap host were measured. High PLQYs of unity were maintained for both films though their significantly redshifted emission peaking at 672 nm and 698 nm for R-BN and R-TBN, respectively, suggesting the strong ability of those molecules in beating the limitation of energy gap law (Supplementary Fig. 11). Also, a relatively larger FWHMs of 48 nm and 49 nm were recorded for R-BN and R-TBN, respectively, partly attributed to the interaction between host and dopant. The TADF characteristics of the R-BN and R-TBN were recorded and depicted in Supplementary Fig. 12. Both prompt and delayed fluorescence components were clearly identified, which can be unambiguously assigned to the TADF emission. The quantum yields ($\phi_F = 0.82$ and $\phi_{DF} = 0.18$ for R-BN, $\phi_F = 0.73$ and $\phi_{DF} = 0.27$ for R-TBN) and lifetimes ($\tau_F = 4.7$ ns and $\tau_{DF} = 0.31$ ms for R-BN, $\tau_F = 10.3$ ns and $\tau_{DF} = 0.71$ ms for R-TBN) of the fluorescence and TADF components were determined based on the total PLQY and ratio of the integrated area of each component in the transient spectra to the total integrated area³⁰. Based on these measurements, the rate constants of fluorescence (k_f), intersystem crossing (k_{ISC}), reverse intersystem crossing (k_{RISC}) and nonradiative transition (k_{nr}) were calculated to be 1.7×10^8 , 3.9×10^7 , 3.9×10^3 s⁻¹, and $<3.3 \times 10^2$ s⁻¹ for R-BN, 7.1×10^7 , 2.6×10^7 , 1.9×10^3 s⁻¹ and $<1.0 \times 10^2$ s⁻¹ for R-TBN, respectively, using the methodology provided in the literature³¹. The large k_f values are consistent with the large molar excitation coefficient ($\log \epsilon = 5.13$ for R-BN and 4.87 for R-TBN, respectively) and large oscillator strengths.

To gain further insight into the nature of electronic excited states, femtosecond pump-probe transient absorption (TA) measurements for R-BN and R-TBN in doped films (3wt% in poly(methyl methacrylate)) were carried out. As shown in Fig. 3d, e, both TA spectra of R-BN and R-TBN showed broad excited-state absorption (EAS) signals, overlapping with two ground state bleach (GSB) bands as well as a stimulated emission (SE) band. Specifically, for R-TBN in doped film, the SE signal at 735 nm rises rapidly and then decay after 3 ps, along with the 675 nm ESA signal decay quickly, corresponding to the vibrational relaxation process from the high vibration levels of S_1 state to the zero vibration level of the S_1 state, and then undergo a ultrafast radiative process within 1.8 ns, in line with its high k_f and PLQY mentioned above. On the other hand, during the following 0.2-10 ps, the $S_0 \rightarrow S_1$ GSB signal around 640 nm exhibited a neglectable peak shift from 641 nm to 645 nm, corresponding to the depopulation of excitons on the vibrational states. This also evidences that both R-BN and R-TBN possess shallow potential energy surface, resulting in the narrow bandwidth emission.

Fig. 4 | OLED performance. a, The energy-level diagrams and the emitter structures of the devices. b, The EL spectra of the optimized DR/NIR devices. c, EQE versus current density characteristics. d, Radiance versus current density characteristics. e, CIE x (left)/EQE (right) summary of DR/NIR TADF-OLEDs with emission peak >650 nm (for references, see Supplementary Table 5).

OLEDs were further constructed to evaluate the performances of those two emitters with the following structures of Indium tin oxide (ITO)/ 1,4,5,8,9,11-hexaazatriphenylene hexacarbonitrile (HATCN, 10 nm)/ 1,1-bis[(di-4-tolylamino)phenyl]cyclohexane (TAPC, 60 nm)/ tris(4-carbazolyl-9-yl)phenyl)amine (TCTA, 10

nm)/ CBP: 30wt% Ir(mphmq)₂tmd: 3wt% R-BN/R-TBN (30 nm)/ 4,6-bis(3-(9H-carbazol-9-yl)phenyl)pyrimidine (CzPhPy, 10 nm)/ 4,6-Bis(3,5-di(pyridin-4-yl)phenyl)-2-methylpyrimidine (B4PyMPM, 50 nm)/ LiF (0.5 nm)/ Al (150 nm). And the device energy levels were provided in Fig. 4a. Electroluminescence spectra with peaks at 664 nm and 686 nm were recorded for R-BN and R-TBN based devices with small FWHMs of 48 nm and 49 nm as illustrated in Fig. 4b, leading to CIE coordinates of (0.719, 0.280) and (0.721, 0.278), respectively. The CIE_x here outperforms all reported values of DR TADF emitters with even red-shifted emission peaks benefiting from their narrow emission bandwidth^{4,13-16,32-38}. For deep red emitters, the radiance is also an important parameter to evaluate their brightness. Maximum radiance of $6.5 \times 10^5 \text{ mW sr}^{-1} \text{ m}^{-2}$ for R-BN and $7.3 \times 10^5 \text{ mW sr}^{-1} \text{ m}^{-2}$ for R-TBN devices were recorded as depicted in Fig.4c. Unprecedentedly high maximum EQEs of 28.4% and 28.1% were observed for R-BN and R-TBN based devices (Fig.4d), respectively. As revealed in Fig. 4e, to the best of our knowledge, those values are the record-high values among all reported results of devices utilizing TADF emitters with peaks >650 nm^{4,13-16,32-38}. Those state-of-the-art performances obtained here testify the great potential of the molecular design strategy.

Discussion

Efficient and bright DR/NIR MR-TADF emitters derived from multiple boron (B) and nitrogen (N) atoms embedded polycyclic heteroaromatics were developed to fundamentally overcome the luminescent boundary set by the 'energy gap law'. By adopting B-phenyl-B and N-phenyl-N structures with mutually ortho-positioned B and N atoms, hybridized π -bonding/ nonbonding molecular orbitals are recorded, not only narrowing energy gap for DR/NIR emission by the delocalized excited states but also eliminating nonradiative transitions by suppressing vibration coupling due to the shallow potential energy curve induced by MR effect. Deep red emitters showed high PLQYs of 100±2% and maximum EQE of >28% with narrow bandwidth emission spectra. This work here provides a strategic implementation of multiple B and N atoms in polycyclic heteroaromatics, showing viable potential to generate DR/NIR emitters with bright and efficient emission without nonradiative transitions. Also, what should be further stressed is that owing to the narrow bandwidth emission, DR/NIR MR-TADF emitters usually exhibit extremely high k_r s, which is indispensable to lower the amplified spontaneous emission (ASE) thresholds in organic DR/NIR lasers.

Methods

Synthesis and characterization. The experimental details on the synthesis and characterization of R-BN and R-TBN are presented in the Supplementary Information.

Single-Crystal Structure. Diffraction data were collected on a Rigaku R-AXIS-RAPID diffractometer using the ω -scan mode with graphite-monochromator Mo•K α radiation. The structure determination was solved with direct methods using the SHELXTL programs and refined with full-matrix least squares on F^2 . The corresponding CCDC reference numbers (2035600 for R-BN and 2035601 for R-TBN) and the data can be

obtained free of charge from The Cambridge Crystallographic Data Centre via www.ccdc.cam.ac.uk/data_request/cif.

Computational methods. The calculations were performed with the Gaussian 09 package, using the density functional theory (DFT) and time-dependent density functional theory (TD-DFT) method with the B3LYP hybrid functional. The structures were optimized using DFT/single-crystals (S_0 states) or TD-DFT (S_1 and T_1 state) methods with a 6-31G(d) basis set. Franck-Condon analyses of the absorption/emission spectra were performed according to the literature³⁹ using the Gaussian 16 package. All calculations were performed in the gas phase.

Measurement of absorption and emission characteristics. 1×10^{-5} M solutions were prepared with 100 mL volumetric flask for all the solution measurements. R-BN/R-TBN:CBP doped films were vacuum evaporated on quartz substrates. UV-vis absorption and PL spectra were measured using UV-2600 (Shimadzu) and FluoroMax-4P (Horiba) instruments at 77 and 298 K. The PLQYs were obtained with an absolute photoluminescence quantum yield measurement system Hamamatsu C9920-03G in an integrating sphere. The solution sample was bubbled with nitrogen for 10 minutes before measurement while the films were measured in air. The transient spectra were collected on an Edinburgh Fluorescence Spectroscopy FLS920 equipped with a R928P photomultiplier tube and a Hamamatsu R5509 near infrared photomultiplier tube. Transient spectra for prompt part were collected with a 442 nm picosecond pulsed LED (EPL450), while the delayed parts were collected with a μ F2 micro-flash lamp.

TPA Measurement: To fabricate the samples for this measurement, the compounds were drop-cast in polymethyl methacrylate (PMMA) at 3 wt%. Sample photoexcitation in the nanosecond transient absorption experiments was achieved by the third harmonic (355 nm) of an electronically triggered Q-switched Nd:YVO4 laser (~ 1 -ns pulse length, Advanced Optical Technologies Ltd AOT-YVO-25QSPX). For the picosecond transient absorption, ~ 100 -fs excitation pulses at 400 nm, generated from the second harmonic of the 800 nm fundamental of the Ti:sapphire laser (Spectra Physics Solstice Ace), were used. The probe was generated by home-built broadband visible (500–770 nm), pumped by the frequency-doubled output (400 nm) of the Ti:sapphire laser. The delay between the pump and probe pulses was varied using a Stanford DG645 delay generator for the nanosecond measurements, whereas a mechanical delay stage (Thorlabs DDS300-E/M) was used to delay the probe with respect to the pump for the picosecond measurements. The transmitted probe pulses were collected with a silicon dual-line array detector (Hamamatsu S8381-1024Q), which was driven and read out by a custom-built board (Stresing Entwicklungsbüro).

Electrochemical measurements. Cyclic voltammetry were performed on a CHI 660 instrument, using a platinum (Pt) electrode as the working electrode, a Pt wire as the auxiliary electrode and an Ag/Ag⁺ electrode as the reference electrode. The oxidation/reduction potentials were measured in dry dichloromethane/DMF solutions with 0.1 M of TBAPF₆ (tetrabutylammonium hexafluorophosphate) as a supporting electrolyte at a scan rate of 100 mV s⁻¹.

$$E_{\text{HOMO}} = - (E_{[\text{onset,ox vs. } \text{Fc}^+/\text{Fc}]} + 4.8) \text{ (eV)}$$

$$E_{\text{LUMO}} = - (E_{[\text{onset,red vs. } \text{Fc}^+/\text{Fc}]} + 4.8) \text{ (eV)}$$

Device fabrication and measurement of EL characteristics. Before device fabrication, the ITO glass substrates were pre-cleaned carefully. Then the sample was transferred to the deposition system. The devices were prepared in vacuum at a pressure of 5×10^{-5} Torr. The hole-injection material HATCN, hole transporting material TAPC, electron-transporting material B4PyMPM, exciton blocking material TCTA and CzPhPy were thermally evaporated at a rate of 1.0 A s^{-1} . After the organic film deposition, 0.5 nm of LiF and 150 nm of aluminum were thermally evaporated onto the organic surface. All of the organic materials used were purified by a vacuum sublimation approach. The current density, voltage, radiant flux, EQE, electroluminescent spectra and other characteristics were measured with a Keithley 2400 source meter and an absolute EQE measurement system in an integrating sphere at the same time. The EQE measurement system is Hamamatsu C9920-12, which equipped with Hamamatsu PMA-12 Photonic multichannel analyzer C10027-02 whose longest detection wavelength is 1100 nm.

Declarations

Acknowledgements ((optional))

This work was supported by the National Key Basic Research and Development Program of China (Grant No. 2016YFB0401003), the National Science Fund of China (Grant Nos. 51525304, 51903137, and 61890942), the China Postdoctoral Science Foundation (Grant No. 2019M650628), the Guangdong Major Project of Basic and Applied Basic Research (Grant No. 2019B030302009) and Foshan Xianhu Laboratory of the Advanced Energy Science and Technology Guangdong Laboratory XHT2020-005.

Author contributions

L.D. and D. D. Z. initiated, designed and supervised the research project and experiments. Y.W.Z. and Y.L. conducted the synthesis and characterization of the compounds. Y.W.Z., T.Y.H., G.M.L., C.Z. and Y.L. performed optical measurements, simulations and calculations. The results were analyzed with the help of Z.Y.B. and J.B.W. A.J.G. and L.S.C. performed transient absorption experiments and data analysis. Y.W.Z., D.D.Z. and Z.Y.L. executed OLED fabrications and analyzed data. The manuscript was written by Y.W.Z. and D.D.Z., and further revised by L.D. All authors discussed the results and contributed to the manuscript.

Competing interests

The authors declare no competing interests.

Data availability

The data that support the plots within this paper and other findings of this study are available from the corresponding author upon reasonable request.

References

1. Caspar, J. V. & Meyer, T. J. Application of the energy gap law to nonradiative, excited-state decay. *Phys. Chem.* **87**, 952-957 (1983).
2. Caspar, J. V. *et al.* Application of the energy gap law to the decay of charge-transfer excited states. *Am. Chem. Soc.* **104**, 630-632 (1982).
3. Takahiko, Y. *et al.* A. Near-infrared organic light-emitting diodes for biosensing with high operating stability. *Phys. Express.***10**, 074101 (2017).
4. Yuan, Y. *et al.* Over 10% EQE near-infrared electroluminescence based on a thermally activated delayed fluorescence emitter. *Funct. Mater.* 1700986 (2017).
5. Tessler, N. *et al.* Efficient near-infrared polymer nanocrystal light-emitting diodes. *Science* **295**, 1506-1508 (2002).
6. Antaris, A. L. *et al.* A small-molecule dye for NIR-II imaging. *Mater.* **15**, 235-242 (2016).
7. Wang, D. *et al.* Highly efficient photosensitizers with far-red/near-infrared aggregation-induced emission for in vitro and in vivo cancer theranostics. *Mater.* **30**, 1802105 (2018).
8. Zampetti, A. *et al.* Near-Infrared (NIR) Organic Light-Emitting Diodes (OLEDs): Challenges and Opportunities. *Funct. Mater.* **29**, 1807623 (2019).
9. Siebrand, W. Radiationless transitions in polyatomic molecules. II: triplet-ground-state transitions in aromatic hydrocarbons. *J. Chem. Phys.* **47**, 2411–2422 (1967).
10. Englman, R. & Jortner, J. The energy gap law for radiationless transitions in large *Mol. Phys.* **18**, 145–164 (1970).
11. Ly, K. T. *et al.* Near-infrared organic light-emitting diodes with very high external quantum efficiency and radiance. *Photon.* **11**, 63–68 (2017).
12. Wei, Y. C. *et al.* Overcoming the energy gap law in near-infrared OLEDs by exciton–vibration decoupling. *Photon.* **14**, 570-577 (2020).
13. Xue, J. *et al.* Highly Efficient Thermally Activated Delayed Fluorescence via J-Aggregates with Strong Intermolecular Charge Transfer. *Mater.* **31**, 1808242 (2019).
14. B. *et al.* Highly Efficient Deep-Red Non-Doped Diodes Based on a T-Shape Thermally Activated Delayed Fluorescence Emitter. *Angew. Chem. Int. Ed.* **59**, 19042-19047 (2020).
15. Yang, T. *et al.* Construction of Efficient Deep-Red/Near-Infrared Emitter Based on a Large π -Conjugated Acceptor and Delayed Fluorescence OLEDs with External Quantum Efficiency of over 20%. *Phys. Chem. C* **123**, 18585-18592 (2019).
16. Kumsampao, J. *et al.* A Simple and Strong Electron-Deficient 5, 6-Dicyano [2,1,3] benzothiadiazole-Cored Donor-Acceptor-Donor Compound for Efficient Near Infrared Thermally Activated Delayed Fluorescence. *-Asian J.* **15**, 3029-3036 (2020).

17. Yasuhiro, K. *et al.* Narrowband deep-blue organic light-emitting diode featuring an organoboron-based emitter. *Photon.* **13**, 678–682 (2019).
18. Hatakeyama, T. *et al.* Ultrapure blue thermally activated delayed fluorescence molecules: efficient HOMO-LUMO separation by the multiple resonance effect. *Mater.* **28**, 2777–2781 (2016);
19. Nakatsuka, S., Gotoh, H., Kinoshita, K., Yasuda, N. & Hatakeyama, T. Divergent synthesis of heteroatom-centered 4,8,12-triazatriangulenes. *Chem. Int. Ed.* **56**, 5087–5090 (2017).
20. Matsui, K. *et al.* One-shot multiple borylation toward BN-doped nanographenes. *Am. Chem. Soc.* **140**, 1195–1198 (2018).
21. Liang, X. *et al.* Peripheral amplification of multi-resonance induced thermally activated delayed fluorescence for highly efficient OLEDs. *Chem. Int. Ed.* **57**, 11316–11320 (2018).
22. Knöllner, J. A. *et al.* Berichtigung: Divergente Synthese von B, N, B-Benzo [4] helicenen durch intramolekulare Borylierung unter sequenzieller B-Mes-Bindungsspaltung. *Chem. Int. Ed.* **132**, 3181–3185 (2020).
23. Xu, Y. *et al.* Constructing Charge-Transfer Excited States Based on Frontier Molecular Orbital Engineering: Narrowband Green Electroluminescence with High Color Purity and Efficiency. *Chem. Int. Ed.* **59**, 17442–17446 (2020).
24. Zhang, Y. *et al.* Multi-Resonance Induced Thermally Activated Delayed Fluorophores for Narrowband Green OLEDs. *Chem. Int. Ed.* **58**, 16912 (2019).
25. Zhang, Y. *et al.* Achieving Pure Green Electroluminescence with CIE_y~0.69 and EQE~28.2% from a Novel Aza-Fused Multi-Resonance Emitter. *Chem. Int. Ed.* **59**, 17499 (2020).
26. Yang, M. *et al.* Full-Color, Narrowband, and High-Efficiency Electroluminescence from Boron and Carbazole Embedded Polycyclic Heteroaromatics. *Am. Chem. Soc.* **142**, 19468–19472 (2020).
27. Noda, H. *et al.* Critical role of intermediate electronic states for spin-flip processes in charge-transfer-type organic molecules with multiple donors and acceptors. *Mater.* **18**, 1084–1090 (2019).
28. Zhang, D. *et al.* Efficient and Stable Deep-Blue Fluorescent Organic Light-Emitting Diodes Employing a Sensitizer with Fast Triplet Upconversion. *Mater.* **32**, 1908355 (2020).
29. Hutchison, G. R., Ratner, M. A. & Marks, T. J. Hopping transport in conductive heterocyclic oligomers: reorganization energies and substituent effects. *Am. Chem. Soc.* **127**, 2339–2350 (2005).
30. Park, I. S. *et al.* High-performance dibenzoheteraborin-based thermally activated delayed fluorescence emitters: molecular architectonics for concurrently achieving narrowband emission and efficient triplet–singlet spin conversion. *Funct. Mater.* **28**, 1802031 (2018).
31. Zhang, D. *et al.* Versatile Indolocarbazole-Isomer Derivatives as Highly Emissive Emitters and Ideal Hosts for Thermally Activated Delayed Fluorescent OLEDs with Alleviated Efficiency Roll-Off. *Mater.* **30**, 1705406 (2018).
32. Furue, R. *et al.* Highly Efficient Red-Orange Delayed Fluorescence Emitters Based on Strong π -Accepting Dibenzophenazine and Dibenzoquinoxaline Cores: toward a Rational Pure-Red OLED Design. *Opt. Mater.* **6**, 1701147 (2018).

33. Li, C. et al. Deep-red to near-infrared thermally activated delayed fluorescence in organic solid films and electroluminescent devices. *Chem. Int. Ed.* **56**, 11525-11529 (2017).
34. Wang, S. et al. Highly efficient near-infrared delayed fluorescence organic light emitting diodes using a phenanthrene-based charge-transfer compound. *Chem. Int. Ed.* **54**, 13068–13072 (2015).
35. Sun, K. et al. Near-infrared thermally activated delayed fluorescent dendrimers for the efficient non-doped solution-processed organic light-emitting diodes. *Electron.* **48**, 389-396 (2017).
36. Kim, D. et al. High-efficiency electroluminescence and amplified spontaneous emission from a thermally activated delayed fluorescent near-infrared emitter. *Photon.* **12**, 98-104 (2018).
37. Chen, J. X. et al. Red/Near-Infrared Thermally Activated Delayed Fluorescence OLEDs with Near 100% Internal Quantum Efficiency. *Chem. Int. Ed.* **58**, 14660-14665 (2019).
38. Zhang, Y. et al. Achieving High-Performance Solution-Processed Deep-Red/Near-Infrared Organic Light-Emitting Diodes with a Phenanthroline-Based and Wedge-Shaped Fluorophore. *Electron. Mater.* **5**, 1800677 (2019).
39. Santoro, F., Lami, A., Improta, R., Bloino, J. & Barone, V. Effective method for the computation of optical spectra of large molecules at finite temperature including the Duschinsky and Herzberg–Teller effect: the Qx band of porphyrin as a case study. *Chem. Phys.* **128**, 224311 (2008).

Figures

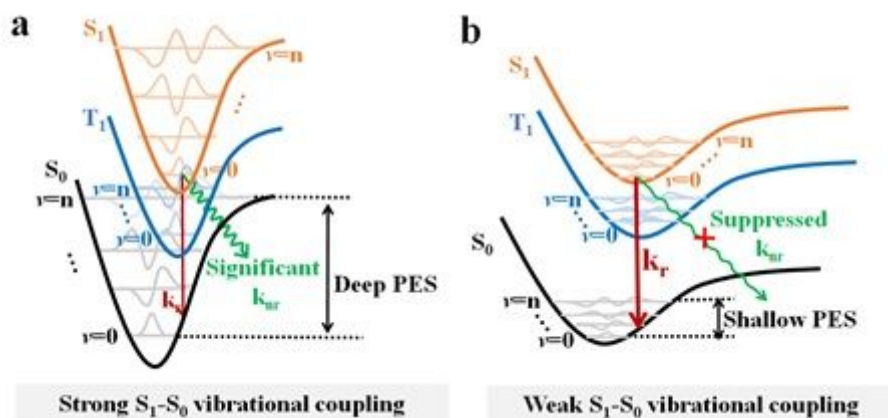


Figure 1

Relationship between PES and excited states decay processes. a, Scheme of excited states decay processes of PAHs with π -bonding and deep PES. In this type emitters, only a few vibrational ladders in S_0 are required to satisfy the energy requirement for vibronic coupling with v_0 of S_1 , drastically increasing nonradiative transitions and reducing the emission intensity. b, Scheme of excited states decay processes of MR TADF emitters with non-bonding and shallow PES. In this type emitters, owing to the reduced vibrational frequency, it is hard for vibrational ladders in S_0 to reach the energy requirement for vibronic coupling with v_0 of S_1 , thus benefiting to eliminate nonradiative transitions.

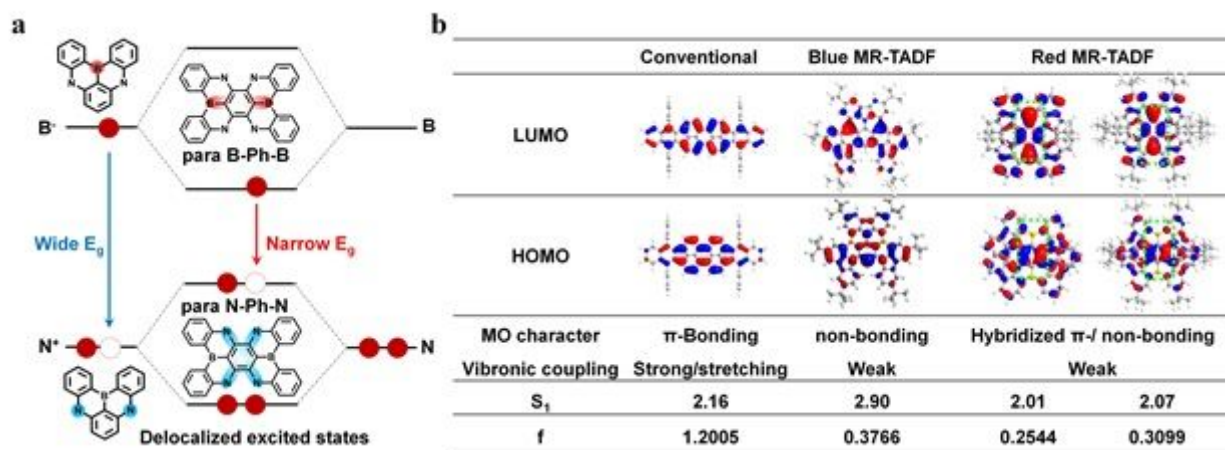


Figure 2

Molecular design strategy of DR/NIR MR-TADF emitters. a, Scheme of the formation of delocalized excited states with B-phenyl-B and N-phenyl-N structures. b, The comparison between conventional PAH, MR-TADF emitters with and without B-phenyl-B and N-phenyl-N structures. For conventional PAH, taking 3,8,13,18-tetraphenylbenzo[5,6]indeno[1,2,3-cd]benzo[5,6]indeno[1,2,3-lm]perylene (DBP) as an example, π -bonds molecular orbitals can be observed. For MR-TADF emitters without B-phenyl-B or N-phenyl-N structures, non-bonding orbitals are obtained.

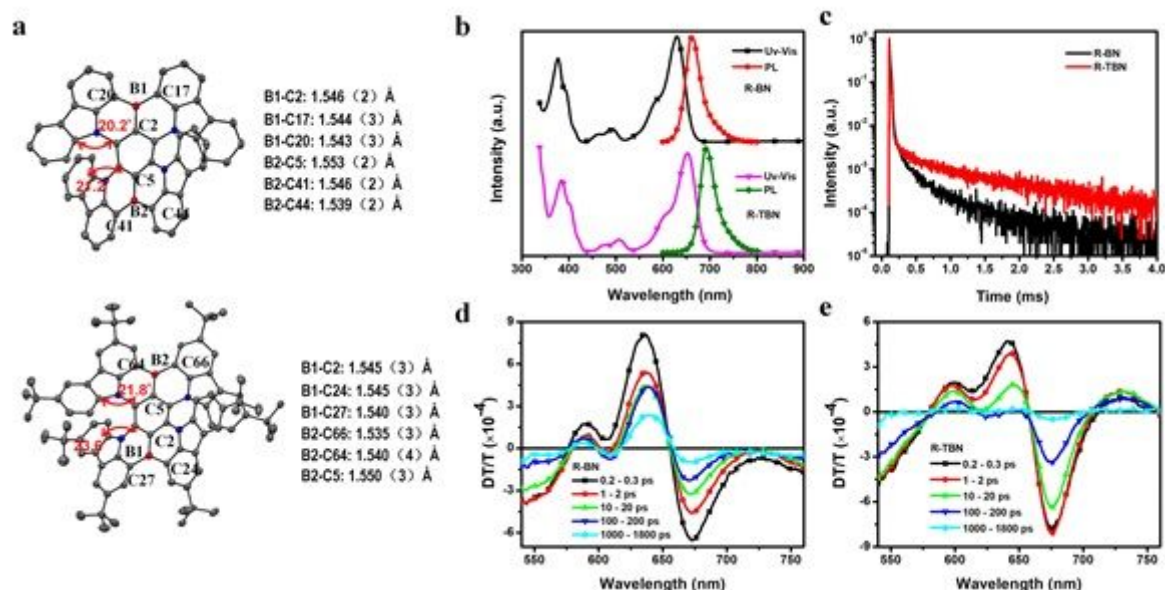


Figure 3

Structure and photophysical properties of R-BN and R-TBN. a, ORTEP drawing of R-BN (up) and R-TBN (down) obtained by X-ray crystallographic analysis. Thermal ellipsoids are shown at 50% probability. Hydrogen atoms are omitted for clarity. b, UV/Vis absorption and fluorescence (298 K) spectra of R-BN and R-TBN in toluene. c, Transient PL decay spectra of R-BN/R-TBN doped into CBP films (3 wt%) at room temperature. d, Transient absorption (TPA) spectra of R-BN (d) and R-TBN (e) doped in PMMA films (3 wt%) at room temperature.

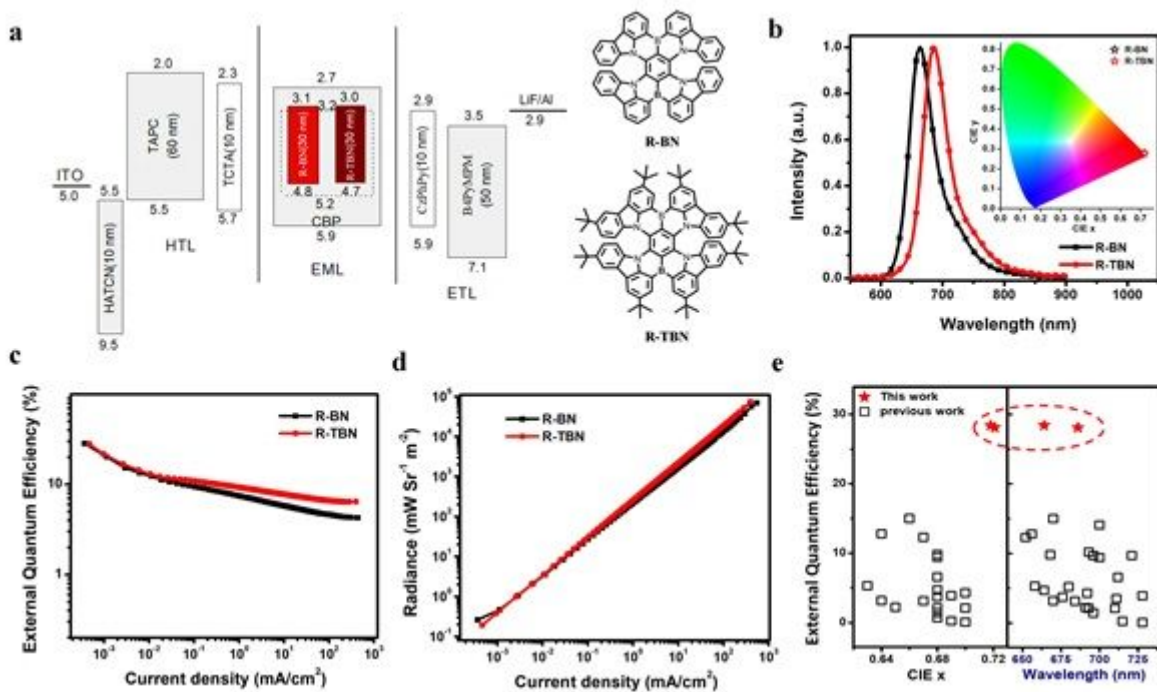


Figure 4

OLED performance. a, The energy-level diagrams and the emitter structures of the devices. b, The EL spectra of the optimized DR/NIR devices. c, EQE versus current density characteristics. d, Radiance versus current density characteristics. e, CIE x (left)/EQE (right) summary of DR/NIR TADF-OLEDs with emission peak >650 nm (for references, see Supplementary Table 5).

Supplementary Files

This is a list of supplementary files associated with this preprint. Click to download.

- [SIRedBNNP.docx](#)